Published in final edited form as:
IEEE Trans Ultrason Ferroelectr Freq Control. 2023 December ; 70(12): 1703–1713. doi:10.1109/TUFFC.2023.3283139.

Dual-Scan Photoacoustic Tomography for the Imaging of Vascular Structure on Foot

Chuqin Huang,
Department of Biomedical Engineering, University at Buffalo, The State University of New York, Buffalo, NY.

Yanda Cheng,
Department of Biomedical Engineering, University at Buffalo, The State University of New York, Buffalo, NY.

Wenhan Zheng,
Department of Biomedical Engineering, University at Buffalo, The State University of New York, Buffalo, NY.

Robert W. Bing,
Department of Biomedical Engineering, University at Buffalo, The State University of New York, Buffalo, NY.

Huijuan Zhang,
Department of Biomedical Engineering, University at Buffalo, The State University of New York, Buffalo, NY.

Isabel Komornicki,
Department of Surgery, University at Buffalo, The State University of New York, Buffalo, NY.

Linda M. Harris,
Department of Surgery, University at Buffalo, The State University of New York, Buffalo, NY.

Praveen R. Arany,
Department of Oral Biology, Biomedical Engineering, & Surgery, University at Buffalo.

Saptarshi Chakraborty,
Department of Biostatistics.

Qifa Zhou [Fellow IEEE],
Department of Biomedical Engineering, University of Southern California, Los Angeles, CA

Wenyao Xu [Member, IEEE],
Department of Computer Science and Engineering.

Jun Xia [Member, IEEE]

Corresponding : junxia@buffalo.edu.
C. Huang and Y. Cheng contributed equally to this work and should be considered as co-first author.

V. Declaration of Competing Interest
Dr. Jun Xia is the founder of Sonioptix, LLC, which, however, did not support this work. All other authors declare no conflicts of interest.

Department of Biomedical Engineering, University at Buffalo, The State University of New York, Buffalo, NY.

Abstract

Chronic leg ulcers are affecting approximately 6.5 million Americans, and they are associated with significant mortality, reduced quality of life, and high treatment costs. Since many chronic ulcers have underlying vascular insufficiency, accurate assessment of tissue perfusion is critical to treatment planning and monitoring. This study introduces a dual-scan photoacoustic tomography system that can simultaneously image the dorsal and plantar sides of the foot to reduce imaging time. To account for the unique shape of the foot, the system employs height-adjustable and articulating base ball stages that can scan along the foot's contour. In vivo results from healthy volunteers demonstrate the system's ability to acquire clear images of foot vasculature, and results from patients indicate that the system can image patients with various ulcer conditions. We also investigated various photoacoustic features and examined their correlation with the foot condition. Our preliminary results indicate that vessel sharpness, occupancy, intensity, and density could all be used to assess tissue perfusion. This research demonstrated the potential of photoacoustic tomography for routine clinical tissue perfusion assessment.

Keywords

Chronic leg ulcers; Foot imaging; Peripheral vascular disorders; Photoacoustic; Photoacoustic tomography

I. Introduction

Chronic leg ulcers are commonly associated with peripheral vascular disorders, and affect approximately 6.5 million Americans [1–3]. Patients with ulcers commonly suffer from decreased mobility and lower quality of life [2]. Revascularization surgery is one of the most effective treatments for ischemia-related foot ulcers, as it restores blood flow and perfusion to the ulcer region. Thus, the ability to monitor the change in perfusion before and after surgery is essential in determining surgical success.

However, current clinical tests fail to meet this need [4]. For instance, ankle-brachial index (ABI) and toe-brachial index (TBI) cannot provide information on perfusion conditions of a specific region; handheld Doppler Ultrasound has limitations due to its low sensitivity to the microvasculature [5]; photoplethysmography (PPG) is affected by skin conditions and its readings cannot be mapped to a single vessel [6]; transcutaneous oxygen (TcPO2) pressure requires a long acquisition time (larger than 30 minutes) and has not been shown to accurately assess perfusion related healing [7]; and X-ray CT angiogram and ICG-based near-infrared fluorescence angiography have ionizing radiation or need contrast agent injection and are not appropriate for monitoring perfusion over time.

Photoacoustic (PA) tomography (PAT) is an emerging imaging modality based on the PA effect [8]. The light energy is transformed into heat during the light absorption in tissue. Meanwhile, mechanical waves, which are generated by the thermoelastic expansion of the tissue, are detected by ultrasonic probes [9]. High-resolution PA images of light absorption can be formed by back projecting PA signals. PAT overcomes the diffusion limit of light and generates high-resolution images in optical diffusive regimes, as acoustic scattering is much weaker than that of light in tissue [9]. For perfusion assessment, the major PA contrast is hemoglobin, and its concentration and distribution are correlated with blood perfusion. Compared to other optical imaging methods for foot assessment, photoacoustic imaging has unique advantages. For instance, direct eye visualization is the most common technique in wound assessment, but it cannot provide functional or depth information. Optical fluorescence imaging has also been used for perfusion assessment [7, 10], however, it needs contrast agent injection. Multi-spectral imaging is another emerging technique [11]. While it provides functional information on blood oxygenation, it cannot reveal the vasculature and depth information. In contrast, PAT enables label-free three-dimensional (3D) imaging of hemoglobin distribution, allowing for safe assessment of the blood perfusion after revascularization surgery.

Over the past few years, various PAT systems have been proposed for imaging foot ulcers. For instance, Yang et *al*. devised a real-time PA/Ultrasound (US) system with an arc-shaped concave transducer array and compared the PA signal intensity with and without occlusion [12, 13]. Taruttis et *al*. proposed a handheld Multispectral optoacoustic tomography (MSOT) with a concave transducer array for imaging both major and microvasculature on foot, providing images of hemoglobin oxygen saturation and pulsation [14]. Mantri et *al*. utilized an LED-based PA system with a linear transducer array to monitor the peripheral hemodynamic response to changes in blood pressure in healthy volunteers and patients undergoing hemodialysis [15]. However, all these systems could only image a cross-section and the selection of the cross-section is operator-dependent. Recently, Choi et *al*. developed a three-dimension (3D) PA/US multistructural quantitative imaging platform with a linear transducer array and the system provides volumetric and multiparametric information about the foot [16]. A potential concern is that the system requires the foot to be fully immersed in water, which could pose a challenge for patients with wounds. Additionally, the system necessitates a longer scanning time as it needs a pre-scan for height estimation. Lee et *al*. demonstrated a compact handheld 3D PA/US scanner that does not need water immersion. However, the motion artifact might impact the imaging quality [17]. Nagae et *al*. built a 3D limb imaging system using a hemispherical detector array. However, the system is relatively bulky and expensive due to the transducer design. In addition, positioning of the foot is not very convenient [18]. Previously, our group also introduced a 3D PAT system for wound assessment, and we demonstrated preliminary results from patients. However, similar to all 3D PAT systems mentioned above, it can only image one side of the foot, while ulcers might occur at multiple locations [19].

Here we introduce a dual-scan 3D PAT system for imaging the vascular structure of the foot. The system is capable of imaging both the dorsal and plantar sides of the foot simultaneously to reduce imaging time. The whole system is built on a cart and takes very little clinical space. To account for the height change on the dorsal side of the foot, we also integrated a laser distance sensor into the motion control system. The performance of our system is demonstrated through phantom imaging and human tests. Our results indicate that the system has a high potential for clinical translation.

II. Methods

A. System Design

The proposed system is comprised of two scanning subsystems, as shown in Fig. 1a. The top subsystem images the instep of the foot, while the bottom subsystem scans the plantar side. The light source is a portable Nd:YAG laser (Big Sky Laser) operating at 10 Hz with a pulse width of about 8 ns and a wavelength of 1064 nm. The laser output is coupled to a bifurcated fiber bundle (Dolan-Jenner Industries) for light delivery to both top and bottom subsystems. PA signals from both subsystems are captured by a 256-channel data acquisition (DAQ) unit (PhotoSound Technologies Inc.) operating at a 40 MHz sampling rate. Synchronization of data capturing and laser pulse is achieved by trigger signals from the laser. The entire system is installed on a mobile cart (McMaster Inc.), as shown in Fig. 1b. An optical breadboard (Thorlabs, Inc) is mounted on the lower level of the cart as the base of the system. The water tank for the bottom subsystem is fixed to the breadboard, whereas the top one is mounted on two position slides (McMaster Inc.), so the top water tank can be moved up and down to fit different foot sizes. Both water tanks are made with clear polycarbonate sheets (McMaster Inc.) and the imaging windows are sealed with 0.001″ plastic films.

The scanning head of the top subsystem consists of a customized linear-array transducer (Imasonic SAS, France) with 128 elements and 2.25 MHz central frequency (named as L2), one of the bifurcated fiber bundle output (3-inch line output), a high-performance cold mirror (Edmund Optics Inc.), and a 3D-printed base. The transducer elements were designed by scaling down the frequency of a clinical L7–5 transducer from 5 MHz to 2.25 MHz. It has an 86 mm total length to cover the region of interest on foot, and each element is curved to achieve acoustic focusing without using a lens. The transducer and fiber bundle head are placed vertically to each other as shown in Fig. 1a, and the cold mirror is attached at 45 degrees to the fiber bundle. This design achieves co-planar light illumination and acoustic detection, offering optimum imaging depth [20]. The scanning head is installed on an articulating baseball stage (Thorlabs Inc.), allowing easy positioning of the head to align with the foot surface. The ball stage is further mounted on two translation stages, which are used for scanning and height adjustment, respectively.

As the bottom scanning head is completely immersed in water, a double mirror structure shown in Fig. 1a is utilized to achieve the co-planar light delivery and acoustic receiving [21]. A high-performance hot mirror (>95% reflection at 1064nm, Edmund Optics Inc.) is mounted in front of the fiber bundle to reflect the light. Another cold mirror is placed parallel to the hot mirror as shown in Fig. 1a, which enables over 90% transmission at 1064 nm and reflects the acoustic waves to the transducer. The bottom linear-array transducer has 128 elements with 5 MHz central frequency and 50 mm lateral length. A higher frequency transducer is used at the bottom as vessels are smaller on the plantar side of the foot. The scanning head is connected to a translation stage and driven by a stepper motor to perform linear scanning.

B. Foot Coupling

Prior to placing the foot on the bottom water tank, we attach a small medical tape on the skin for better correlation of the PA imaging region with the photos. The tape has a cross-shaped black mark, which can be visualized in PA. Then, we apply ultrasound gel on the plantar side of the foot filling the gaps between the toes to enhance acoustic coupling. For patients with foot ulcers, we used sterilized clear Gel (AquaSonic clear, Parker Laboratories, Inc.) to reduce the risk of infection. The plantar side of the patient's foot is mostly flat, so the bottom water tank has a flat imaging window covered by a plastic membrane (Fig. 2a).

The top imaging window has a slope to account for the height difference between the toes and ankle. Based on prior research [22], the average foot size length of an elderly American is 255.9 mm and the average instep height is 114 mm, leading to a 24-degree slope. We chose to design a 15-degree tilted imaging window, as the smaller angle will improve coupling. Once the patient places their foot on the bottom water tank, more ultrasound gel is applied on the instep side. Then, the top water tank is lowered for coupling. The movement of the top water tank is manually controlled by two translation stages. As the top water tank is lowered, the foot instep surface is slightly compressed by the membrane on the water tank to improve acoustic coupling.

The limited view natural of a linear array indicates that the optimal performance of the system is achieved when the array surface is aligned with the object. As the foot instep surface is not flat, we used the articulating platform to manually control transducer positioning before scanning. As depicted in Fig. 2a, the rotation angle is determined manually based on the shape of the foot instep. After the foot coupling procedures have been completed, we can begin scanning with the motion control system.

C. Motion Control

During the experiment, both the top and bottom transducers move simultaneously at a constant scanning speed of 1 mm/s. The height change in the foot instep also brings a challenge in scanning. To ensure that the transducer focus always stays around the skin surface, we used a laser distance sensor (TOF 10102, OCESTORE, US) to estimate the instep height, which is used to guide the scanning. As shown in Fig. 2a, the laser distance sensor is attached to the edge of the top water tank. The laser distance sensor measures and records the instep ankle height. Then, the information is sent to the Arduino program to calculate the endpoint position for the top transducer. This design allows the travel path to vary with ankle heights to ensure that the transducer's focus stays near the foot surface.

D. Image reconstruction and processing

As the Photosound system does not offer real-time display, we transferred raw channel data into the computer for offline processing and reconstruction. We first filter the data by a bandpass filter (1–5 MHz for the top and 3–7 MHz for the bottom) to eliminate noise and then use the back project algorithm to reconstruct the PA image [23]. The 2D image frames are then stacked along the scanning direction to form a 3D image. A wavelet filter is further used to remove electromagnetic interference noises, which is shown as stripes in the reconstructed images [24]. For better visualization, we use the depth-encoded maximum projection image (MAP) to display the 3D image in 2D.

We also noticed that the PA surface signal could be high in subjects with dark skin color. Therefore, we developed a skin removal algorithm to reveal the underlying vessels. The algorithm requires the operator to manually pick multiple points in reconstructed data to label the border between the skin and tissue, as shown in Fig. 3. The operation is performed on the axial-lateral plane first to extract the lateral contour of the foot (Fig. 3a and blue line in Fig. 3e), and then the same operation is applied on the axial-elevation plane to get the elevation contour of the foot (Fig. 3d and orange line in Fig. 3e). A 3D skin map is then generated by sweeping the lateral contour along the elevation curve as shown in Fig. 3e. The skin map will be projected to the reconstruction space to mark the regions where the signal will be removed. Fig. 3b shows a PA image of a patient with dark skin, where strong surface signals can be observed. Fig. 3c shows the PA image after skin removal, where the subdermal vasculature structure can be visualized. The manually picked points are shown in Fig. 3a and 3d.

To quantify PA features of tissue perfusion, we extract the vessels in the PAT images for further analysis. The detailed steps are listed in Fig. 4. We first apply the Frangi filter [25] on the grayscale MAP images to improve the vessel contrast and then use the contrast-limited adaptive histogram equalization (CLAHE) to further enhance signals from deeper depths [26]. The resulting image is smoothed with a moving average filter to remove noise [27]. Then, segmentation is performed on the post-processed image to create a vessel mask, based on the threshold obtained by the ISODATA clustering algorithm [27, 28].

Once the vessel mask is acquired, we compute the convex hull using Matlab's built-in function, bwconvhull, to label the region of interest (ROI). Meanwhile, the marker area (on the medical tape) is also identified and will be excluded from the analysis. Four PA-related features are studied to evaluate the perfusion condition within these areas. The first feature is the PA intensity ratio, which is calculated as the ratio of the mean intensity of PA signals within the vessel mask of the healthy foot to that of the foot with ulcers. This feature is related to the total hemoglobin concentration. The second feature is blood vessel occupancy (VO), which is evaluated by calculating the ratio of vessel region to the whole ROI. The third feature is vessel density, which is related to vessel occupancy. In contrast, vessel density quantifies the number of vessels instead of the area of vessels. To do so, we extract the centerline of the vessels using the MATLAB built-in function bwskel [29, 30]. The vessel density (VD) is then calculated by dividing the number of vessel pixels by the ROI. The last feature is vessel sharpness, as quantified based on Equation 1 shown below [31].

$$Sharpness = \frac{\sum \sqrt{G_x^2 + G_y^2}}{Area \times Vessel\ density} \tag{1}$$

Where G_x and G_y are the gradients of the image along horizontal and vertical directions, respectively, and $Area$ is the total number of pixels in the ROI. Chronic wounds are often associated with leaking vessels [32], which might cause blurry edges of vessels. For better comparison across features, the calculated PA intensity is divided by 10^5, and the sharpness index is multiplied by 10^2 in this work.

We also investigated the possibility of integrating different vessel features into a single index. The proposed equation is shown in Equation 2. Here, the coefficient for each feature is the reciprocal of the average indices from healthy volunteers. The coefficients are used to normalize the features. As the vasculature on the instep and sole exhibit different characteristics, the coefficients are determined independently for the top and bottom systems [33].

$$Integrated\ index = \begin{cases} 2.68 \times VO + 1.37 \times \ sharpness \ + 0.52 \times VD, & \text{for } top \\ 2.07 \times VO + 0.83 \times \ sharpness \ + 0.27 \times VD, & for\ bottom \end{cases} \quad (2)$$

III. Results

A. Resolution quantification

To quantify system resolution, we used a 0.2 mm width cross-line phantom made by a laser printer. The phantom was placed on a 3D-printed foot to mimic the experimental environments. A ballistic gel pad was placed between the foot and phantom for better coupling. The distance from the phantom to the transducer is around 4 cm, which is the focal distance of the transducer. PA images of the phantom from the top and bottom systems are shown in Fig. 5a and 5b, respectively. The spatial resolution was quantified based on the full width at half maximum (FWHM) of the reconstructed image. The pixels used for resolution quantification are marked in the PA reconstructed images, where the red line marks lateral and the green line labels elevation. The lateral resolution was quantified to be 0.77 mm and 0.54 mm for the top system and bottom systems as shown in Fig. 5c and 5d, respectively. As indicated in Fig. 5e and 5f, the elevation resolutions are 1.20 mm, and 0.87 mm for the top system and bottom systems, respectively.

B. Healthy Volunteer Results

1): Volunteer Characteristics—The methodology, data, and consent forms for healthy human subjects used in this research were approved by the IRB committee at the University at Buffalo. We recruited 4 healthy volunteers, and all volunteers signed the experiment consent form to collect foot image data. None of the volunteers has foot ulcers or health problems related to the foot.

2): Human Foot Imaging Protocols—Before clinical testing, we tested system usability and robustness with healthy volunteers. The scanning length of the foot instep was 50 mm along the elevation direction from toes to ankle, with a step size of 0.1 mm. The lateral imaging length covered 86 mm from the big toe to the small toe. The scan range of the bottom was 50 mm from toes to arch, with a step size of 0.1 mm. The lateral imaging length covered 50 mm from the big toe to the small toe. The imaging acquisition time was

50 seconds, and the entire imaging session took only 20 minutes from the subject's arrival to dismissal.

3): In-Vivo results from the Healthy Volunteer—Fig. 6a and 6b show the results of two volunteers with a foot size of 10 and 8.5 (US size), respectively. Two groups of scanning were performed on both the dorsal side and plantar side of the foot, and the approximate scanning regions are labeled with blue (for the top system) and orange rectangles (for the bottom system). Depth-encoded MAP images are shown in Figs. 6c–f. The results indicate that our system is capable of providing vascular information on both sides of the foot simultaneously. The vessel features are evaluated for healthy subjects, and the results are listed in Table 1. Based on our results, the vessel density, sharpness, and occupancy are all higher at the plantar side of the foot, while PA intensity is higher at the dorsal side, as the dorsal skin is thinner which attenuates less light [34].

C. Patient imaging results

The proposed system is also tested in the clinic (UBMD vascular surgery, Amherst, NY) by imaging patients with ulcers. The inclusion criterion is any person 18 years of age or older with one or multiple chronic wounds on the foot which is related to arterial perfusion insufficiency or gangrene. Pregnant women and adults unable to consent are excluded from the study. The ABI and TBI measurements are conducted before PA experiments by the clinicians.

Patient 1 is a 68-year-old male with a femoral artery aneurysm and gangrene on the toe of the left foot. PA imaging is performed on both left and right feet for comparison. As shown in Fig. 7a and 7b, the scanning region (calibrated based on the marker) is labeled with a blue rectangle for the top systems. A chronic ulcer is observed on the bottom of the left foot, as shown in Fig. 7c. The ulcer has mostly healed based on clinical records. PA imaging results are shown in Fig. 7d–7g. The Ankle Brachial Index (ABI) and Toe Brachial Index (TBI), acquired before the PA experiments, are listed in Fig. 7d and 7e, showing that the perfusion condition is similar in both feet. The vessel features are quantified, and the results are listed in Table 2. It can be seen that the index of most features in the top of the right foot (healthier foot) is higher than the left one, which agrees with the foot condition and ABI and TBI test results. For the bottom imaging results, the left foot has a lower integrated index than the right one, though the vessel occupancy and vessel density show different trends.

Patient 2 is a 52-year-old male with right tranmetatarsal amputation due to ulcers as Fig. 8a and 8b show. In addition, the subject has an open wound on the side of the left foot. PA imaging result from the dorsal side of the left (open wound observed) foot is shown in Fig. 8c, while the dorsal PA image of the foot with amputation is shown in Fig. 8d. Similar to patient 1, we quantified the vessel features and listed the results in Table 2. For most vessel features, the foot with better perfusion condition (left) has much higher values than the amputated one (right). Our system needs further development to acquire the bottom image with this special wound case.

Patient 3 is an 84-year-old patient with chronic ulcers and toe amputation. The photos of the foot and results from the PAT system are shown in Fig. 9. The scanning window is set to cover the region with amputation (Fig. 9a and 9b). The vessel features are evaluated within the region and the results are shown in Table 3. The indices of the amputated foot (left) are smaller than the healthier one (right), except for the vessel occupancy index on the dorsal side. A 3D rendering of the foot vasculature can be found in supplementary materials.

IV. Discussion and Conclusion

In this study, we developed a dual-scan PAT system to image the vascular structures of the foot and use that information to predict perfusion, which could facilitate clinical decision making. The top and bottom subsystem design increases the available imaging region and shortens the scanning time. As Fig. 2b shows, the current system can cover at least half of the foot, allowing it to handle various ulcer positions. For better scanning of the foot, we implemented several mechanisms, such as the adaptive height adjustment, customized water tank with a slope, and the ball stage for better alignment of the transducer. Moreover, the top and bottom systems can work independently, providing more flexibility for wound imaging.

Compared to the existing cross-sectional PAT system for foot imaging [12–15], the proposed design utilizes two linear transducer arrays to image the dorsal and plantar sides of the foot simultaneously. Therefore, our system provides a larger field of view. In addition, the scanner is driven by the translation stage, which reduces the motion artifacts from the freehand operation. Compared to other 3D foot imaging systems, the linear transducer array used in our system has a lower cost [18]. While there are also some linear-array-based 3D foot imaging systems [16, 17], our proposed design used sterilized ultrasound gel instead of water for coupling. It reduces the imaging preparation time and the risk of cross-contamination between patients.

To better evaluate perfusion condition, we quantified four vessel features: PA intensity ratio, vessel occupancy, vessel sharpness, and vessel density. These features are calculated by an automated algorithm, eliminating the influence of subjective manual operation. The PA intensity ratios are larger than 1 in most patient cases, showing that healthier feet have better tissue perfusion. However, we could not compare the PA intensity among patients as the skin condition and color affects the subdermal optical fluence. A more robust PA intensity measure could be investigated in the future to mitigate the skin effect. We compare the PA intensity ratio among patients (healthier foot/ulcer foot) and healthy volunteers (left/right), and the result indicates that the intensity ratio is close to 1 for healthy volunteers while the result from patients is larger than 1. The integrated index of vessel features proposed in this study provides a single number for easy clinical use. We compared these indices of the healthier and ulcered feet of the same patient and found that the indices are smaller in the ulcered foot in most cases. For better visualization, we upload the indices into box plots. As shown in Fig. 10, the integrated indices of healthy volunteers are larger than that of patients, regardless of the presence of the ulcer. Since peripheral artery disease is a systemic disorder, it is likely that the foot without an ulcer also has abnormal perfusion. Among patients, the indices from feet without ulcers are generally larger than that of feet with ulcers, which agrees with clinical observation. Thus, the four vessel features applied in this study have the potential to be used in further clinical studies to predict tissue perfusion. We also noticed that vessel occupancy and vessel density show a similar tendency though they indicate different information. The vessel density represents the number of vessels, whereas the vessel occupancy demonstrates not only the numbers but also the volume of the vessels. In comparison to traditional methods such as ABI/TBI tests, the proposed system can obtain information in a specific region close to the wound, allowing clinicians to gain a better understanding of the tissue perfusion. In addition, the ABI/TBI test is sometimes impeded by amputations or other foot conditions, such as in patient 3, while the PAT system can acquire the vessel information in wider clinical conditions.

In this study, a skin removal algorithm has been developed by manually marking the skin boundary along both lateral and elevational cross-sections, as the skin pigment plays a key role in photoacoustic imaging quality. The subdermal vasculatures are clearly visible after removing the skin layer as shown in Fig. 3. While we have not recruited any patients with dark skin, we expected that the algorithm will perform well in such patients since the skin signal would be easier to identify. However, the ultimate imaging depth could be affected due to strong skin attenuation. Nonetheless, given that most foot ulcers are superficial, adequate signals for feature extraction and quantification should still be attainable.

While promising results have been demonstrated, further improvements in both hardware and software can be implemented. For the hardware, the water tank design can be improved to fit the shape of the foot better, leading to a large field of view with improved coupling. In addition, the current system uses a flashlamp-pumped laser, which is bulky as it requires water cooling. Diode-pumped lasers [35] can be used to further reduce the system size. Furthermore, multi-spectral PA imaging can be implemented for the quantification of blood oxygenation, which is also related to perfusion [11].

In terms of software, the calculated PA indices are both system and patient dependent. Variations in system parameters, such as spatial resolution and excitation wavelength, as well as fluctuations in patient condition, would affect the quantification results. A normalization factor can be developed in the future to neutralize these dependencies and make the quantification results more universally applicable. Moreover, advanced image reconstruction and processing methods can be implemented to reduce image noise and improve spatial resolution [36–38]. Such improvements would allow for more precise quantification of vessel occupancy. A cleaner image will also enable the quantification of vessel curvature, which is relevant to perfusion [39]. Finally, the proposed calculation method can be optimized with more clinical data with proper weighting on different indices to provide a more accurate prediction for tissue perfusion. We also plan to include more PAD control patients without foot ulcers in order to evaluate the potential of our technique for early ulcer detection.

In conclusion, a compact dual-scan 3D PAT system is proposed in this study. The system can simultaneously image both dorsal and plantar sides of the foot, leading to a short scanning time. Co-planar light illumination and acoustic detection are achieved on both the top and bottom subsystems to increase imaging depth. In addition, we used an adaptable height scan on the top system to ensure the feature of interest is always near the transducer focus. The resolution of the system has been quantified with the crossline phantoms. The in-vivo results from healthy volunteers indicate that the system can acquire clear images of foot vascular structure in less than 1 minute of scanning time. Preliminary results from patients with chronic wounds demonstrate the capability of the system to image the vessels of the patients under different situations. Four vessel features from PA images are extracted for analysis, an integrated index is proposed for easy clinical use, and most of the results correlate with the foot condition. As an ongoing study, more patient data will be added in the future to further enhance the accuracy and robustness of our technique, making it a valuable tool for foot ulcer evaluation.

Acknowledgments

This work was supported by the National Institute of Health under Grant R01EB029596 and Grant R01EB028978.

References

[1]. Wang Y, Zhan Y, Harris LM, Khan S, and Xia J, "A portable three-dimensional photoacoustic tomography system for imaging of chronic foot ulcers," Quantitative imaging in medicine and surgery, vol. 9, no. 5, p. 799, 2019. [PubMed: 31281775]

[2]. Sen CK et al. , "Human skin wounds: a major and snowballing threat to public health and the economy," Wound repair and regeneration, vol. 17, no. 6, pp. 763–771, 2009. [PubMed: 19903300]

[3]. Boyko EJ, Monteiro-Soares M, and Wheeler SG, "Peripheral arterial disease, foot ulcers, lower extremity amputations, and diabetes," Diabetes in America. 3rd edition, 2018.

[4]. Ma KF, Kleiss SF, Schuurmann RC, Bokkers RP, Ünlü Ç, and De Vries J-PP, "A systematic review of diagnostic techniques to determine tissue perfusion in patients with peripheral arterial disease," Expert review of medical devices, vol. 16, no. 8, pp. 697–710, 2019. [PubMed: 31340684]

[5]. FrykbergRobert G, "Challenges in the treatment of chronic wounds," Advances in wound care, 2015.

[6]. Allen J, "Photoplethysmography and its application in clinical physiological measurement," Physiological measurement, vol. 28, no. 3, p. R1, 2007. [PubMed: 17322588]

[7]. Venermo M et al. , "Pilot assessment of the repeatability of indocyanine green fluorescence imaging and correlation with traditional foot perfusion assessments," European Journal of Vascular and Endovascular Surgery, vol. 52, no. 4, pp. 527–533, 2016. [PubMed: 27486005]

[8]. Wang LV and Hu S, "Photoacoustic Tomography: In Vivo Imaging from Organelles to Organs," Science, vol. 335, no. 6075, pp. 1458–1462, 2012, doi: doi:10.1126/science.1216210. [PubMed: 22442475]

[9]. Xia J, Yao J, and Wang LV, "Photoacoustic tomography: principles and advances," (in eng), Electromagn Waves (Camb), vol. 147, pp. 1–22, 2014, doi: 10.2528/pier14032303.

[10]. Settembre N, Kauhanen P, Albäck A, Spillerova K, and Venermo M, "Quality control of the foot revascularization using indocyanine green fluorescence imaging," World journal of surgery, vol. 41, pp. 1919–1926, 2017. [PubMed: 28265729]

[11]. Saiko G, Lombardi P, Au Y, Queen D, Armstrong D, and Harding K, "Hyperspectral imaging in wound care: a systematic review," International Wound Journal, vol. 17, no. 6, pp. 1840–1856, 2020. [PubMed: 32830443]

[12]. Yang J, Zhang G, Wu M, Shang Q, Huang L, and Jiang H, "Photoacoustic assessment of hemodynamic changes in foot vessels," Journal of biophotonics, vol. 12, no. 6, p. e201900004, 2019. [PubMed: 30916865]

[13]. Yang J, Zhang G, Shang Q, Wu M, Huang L, and Jiang H, "Detecting hemodynamic changes in the foot vessels of diabetic patients by photoacoustic tomography," Journal of biophotonics, vol. 13, no. 8, p. e202000011, 2020. [PubMed: 32362070]

[14]. Taruttis A, Timmermans AC, Wouters PC, Kacprowicz M, van Dam GM, and Ntziachristos V, "Optoacoustic imaging of human vasculature: feasibility by using a handheld probe," Radiology, vol. 281, no. 1, pp. 256–263, 2016. [PubMed: 27379543]

[15]. Mantri Y, Dorobek TR, Tsujimoto J, Penny WF, Garimella PS, and Jokerst JV, "Monitoring peripheral hemodynamic response to changes in blood pressure via photoacoustic imaging," Photoacoustics, vol. 26, p. 100345, 2022. [PubMed: 35295617]

[16]. Choi W et al. , "Three-dimensional multistructural quantitative photoacoustic and US imaging of human feet in vivo," Radiology, vol. 303, no. 2, pp. 467–473, 2022. [PubMed: 35191741]

[17]. Lee C, Choi W, Kim J, and Kim C, "Three-dimensional clinical handheld photoacoustic/ ultrasound scanner," Photoacoustics, vol. 18, p. 100173, 2020. [PubMed: 32215250]

[18]. Nagae K et al. , "Real-time 3D photoacoustic visualization system with a wide field of view for imaging human limbs," F1000Research, vol. 7, 2018.

[19]. Agale SV, "Chronic leg ulcers: epidemiology, aetiopathogenesis, and management," Ulcers, vol. 2013, 2013.

[20]. Montilla LG, Olafsson R, Bauer DR, and Witte RS, "Real-time photoacoustic and ultrasound imaging: a simple solution for clinical ultrasound systems with linear arrays," Physics in Medicine & Biology, vol. 58, no. 1, p. N1, 2012.

[21]. Wang Y, Lim RSA, Zhang H, Nyayapathi N, Oh KW, and Xia J, "Optimizing the light delivery of linear-array-based photoacoustic systems by double acoustic reflectors," Scientific reports, vol. 8, no. 1, pp. 1–7, 2018. [PubMed: 29311619]

[22]. Tomassoni D, Traini E, and Amenta F, "Gender and age related differences in foot morphology," Maturitas, vol. 79, no. 4, pp. 421–427, 2014. [PubMed: 25183323]

[23]. Xu M and Wang LV, "Universal back-projection algorithm for photoacoustic computed tomography," Physical Review E, vol. 71, no. 1, p. 016706, 2005.

[24]. Münch B, Trtik P, Marone F, and Stampanoni M, "Stripe and ring artifact removal with combined wavelet—Fourier filtering," Optics express, vol. 17, no. 10, pp. 8567–8591, 2009. [PubMed: 19434191]

[25]. Frangi AF, Niessen WJ, Vincken KL, and Viergever MA, "Multiscale vessel enhancement filtering," in International conference on medical image computing and computer-assisted intervention, 1998: Springer, pp. 130–137.

[26]. Zuiderveld K, "Contrast limited adaptive histogram equalization," Graphics gems, pp. 474–485, 1994.

[27]. Madasamy A, Gujrati V, Ntziachristos V, and Prakash J, "Deep learning methods hold promise for light fluence compensation in three-dimensional optoacoustic imaging," Journal of biomedical optics, vol. 27, no. 10, p. 106004, 2022. [PubMed: 36209354]

[28]. Ridler T and Calvard S, "Picture thresholding using an iterative selection method," IEEE trans syst Man Cybern, vol. 8, no. 8, pp. 630–632, 1978.

[29]. Kerschnitzki M et al. , "Architecture of the osteocyte network correlates with bone material quality," Journal of bone and mineral research, vol. 28, no. 8, pp. 1837–1845, 2013. [PubMed: 23494896]

[30]. Lee T-C, Kashyap RL, and Chu C-N, "Building skeleton models via 3-D medial surface axis thinning algorithms," CVGIP: Graphical Models and Image Processing, vol. 56, no. 6, pp. 462–478, 1994.

[31]. Cruz G, Atkinson D, Henningsson M, Botnar RM, and Prieto C, "Highly efficient nonrigid motion-corrected 3D whole-heart coronary vessel wall imaging," Magnetic resonance in medicine, vol. 77, no. 5, pp. 1894–1908, 2017. [PubMed: 27221073]

[32]. Shaterian A et al. , "Real-time analysis of the kinetics of angiogenesis and vascular permeability in an animal model of wound healing," Burns, vol. 35, no. 6, pp. 811–817, 2009. [PubMed: 19423227]

[33]. Eizenberg N, Briggs C, Adams C, and Ahern G, "General anatomy: Principles and applications," 2008.

[34]. Sowers T, Yoon H, and Emelianov S, "Investigation of light delivery geometries for photoacoustic applications using Monte Carlo simulations with multiple wavelengths, tissue

types, and species characteristics," Journal of biomedical optics, vol. 25, no. 1, p. 016005, 2020. [PubMed: 31975577]

[35]. Wang D et al. , "Deep tissue photoacoustic computed tomography with a fast and compact laser system," Biomedical optics express, vol. 8, no. 1, pp. 112–123, 2017. [PubMed: 28101405]

[36]. Xia J et al. , "Three-dimensional photoacoustic tomography based on the focal-line concept," Journal of Biomedical Optics, vol. 16, no. 9, p. 090505, 2011. [Online]. Available: 10.1117/1.3625576. [PubMed: 21950908]

[37]. Zhang H et al. , "Deep-E: A fully-dense neural network for improving the elevation resolution in linear-array-based photoacoustic tomography," IEEE Transactions on Medical Imaging, vol. 41, no. 5, pp. 1279–1288, 2021.

[38]. Zheng W et al. , "Deep-E Enhanced Photoacoustic Tomography Using Three-Dimensional Reconstruction for High-Quality Vascular Imaging," Sensors, vol. 22, no. 20, p. 7725, 2022. [PubMed: 36298076]

[39]. Matsumoto Y et al. , "Label-free photoacoustic imaging of human palmar vessels: a structural morphological analysis," Scientific reports, vol. 8, no. 1, pp. 1–8, 2018. [PubMed: 29311619]

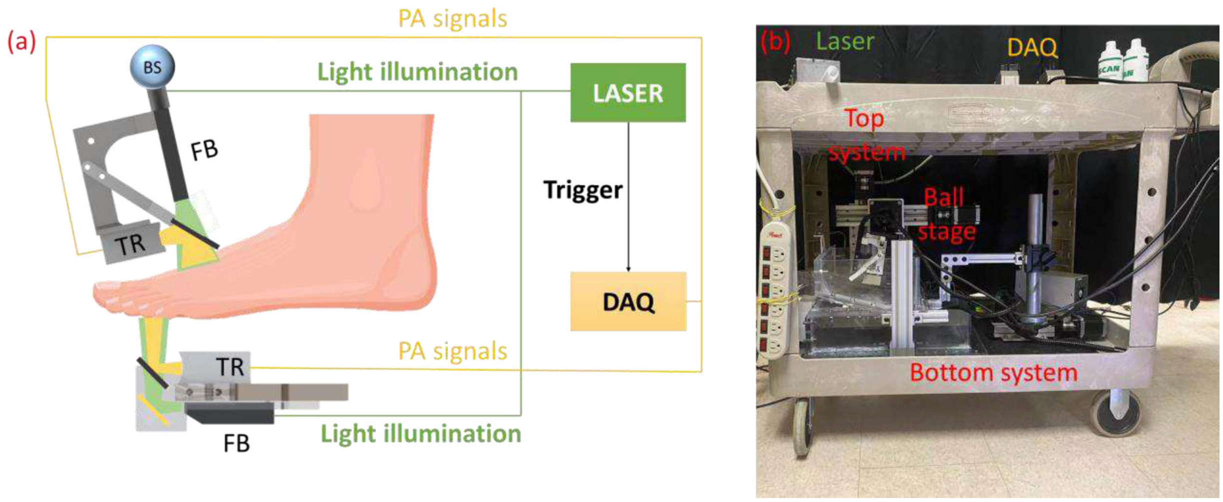

Fig. 1.

Experimental setup of the dual-scan imaging system. (a) A schematic drawing of the dual-scan PAT system. The light transmission is marked in green, while the acoustic propagation is labeled in yellow. BS: Ball stage; FB: fiber bundle; TR: transducer. (b) A photograph of the system. Most equipment is installed on a cart except the portable laser.

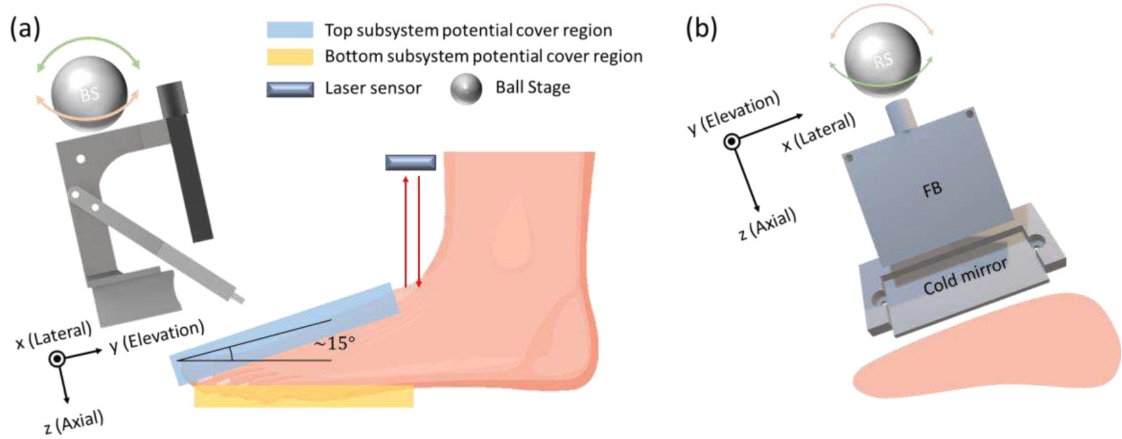

Fig. 2.

Schematic drawings of the top and bottom scanning schemes. (a) A schematic drawing in axial-elevation view of the transducer. The laser distance sensor is mounted close to the ankle to measure the distance from the sensor to the skin surface. The potential scanning regions are marked with blue and yellow for the top and bottom systems, respectively. The scanner is rotated via the ball stage in the axial-elevation plane to align with the foot. (b) A schematic drawing in the axial-lateral view of the transducer. The transducer is positioned parallel to the lateral direction, covering from the right (big toe) to the left (small toe). The scanner can also be manually rotated in the axial-lateral plane to fit the curve of the foot.

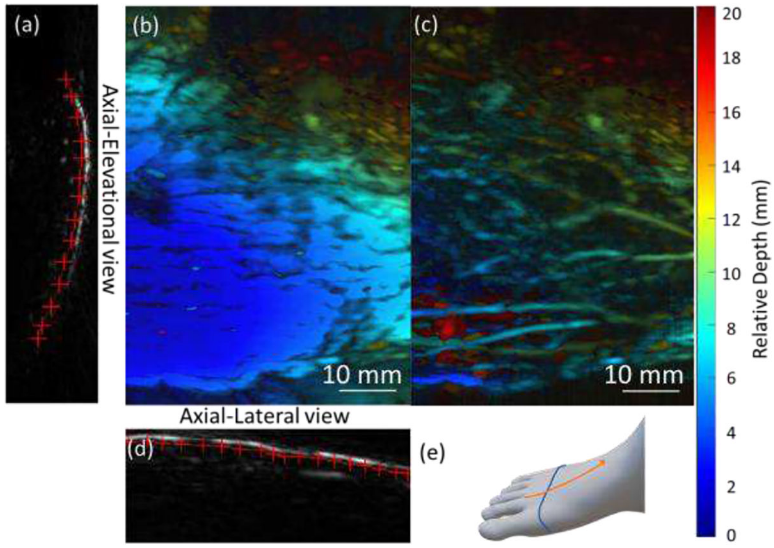

Fig. 3.

Demonstration of the skin removal algorithm. (a) Manual selection of the skin region in axial-lateral cross-sectional view. (b) A PA depth-encoded maximum amplitude projection (MAP) image of the subject's foot. The skin signal has strong intensity, making it hard to see vessels beneath the skin. (c) A PA depth-encoded MAP image after the skin removal algorithm. The vessels can now be clearly visualized. (d) Manual selection of the skin region in axial-elevation cross-sectional view. (e) A schematic drawing of the foot and the curves used to mark the skin. The blue curve shows the cross-section profile of the foot and the orange curve shows the height change of the foot.

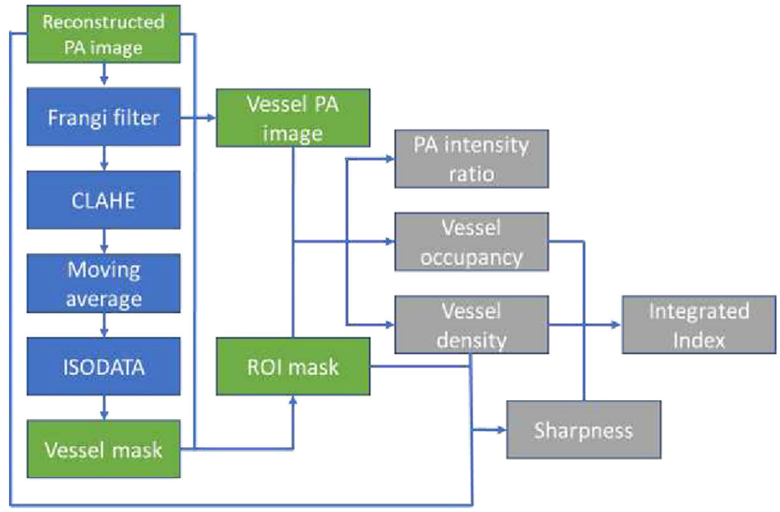

Fig. 4.

A flowchart of the feature extraction procedure.

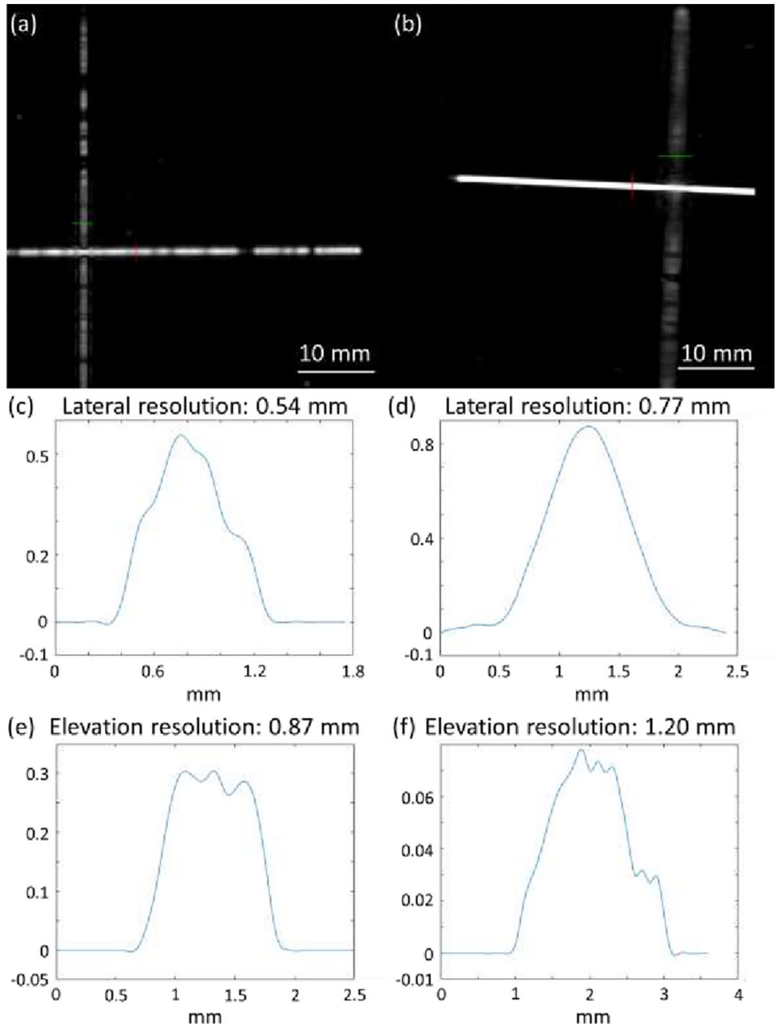

Fig. 5.

Quantification of the system's spatial resolution. (a) A Maximum Amplitude Projection (MAP) image of the cross-line phantom acquired by the bottom system. (b) A MAP image of the cross-line phantom acquired by the top system. The resolution is quantified by Full-Width at Half Maximum (FWHM). (c)-(d) The lateral resolutions are 0.54 mm and 0.77 mm in the bottom and top systems, respectively. (e)-(f) The elevation resolutions are 0.87 mm and 1.20 mm in the bottom and top systems, respectively.

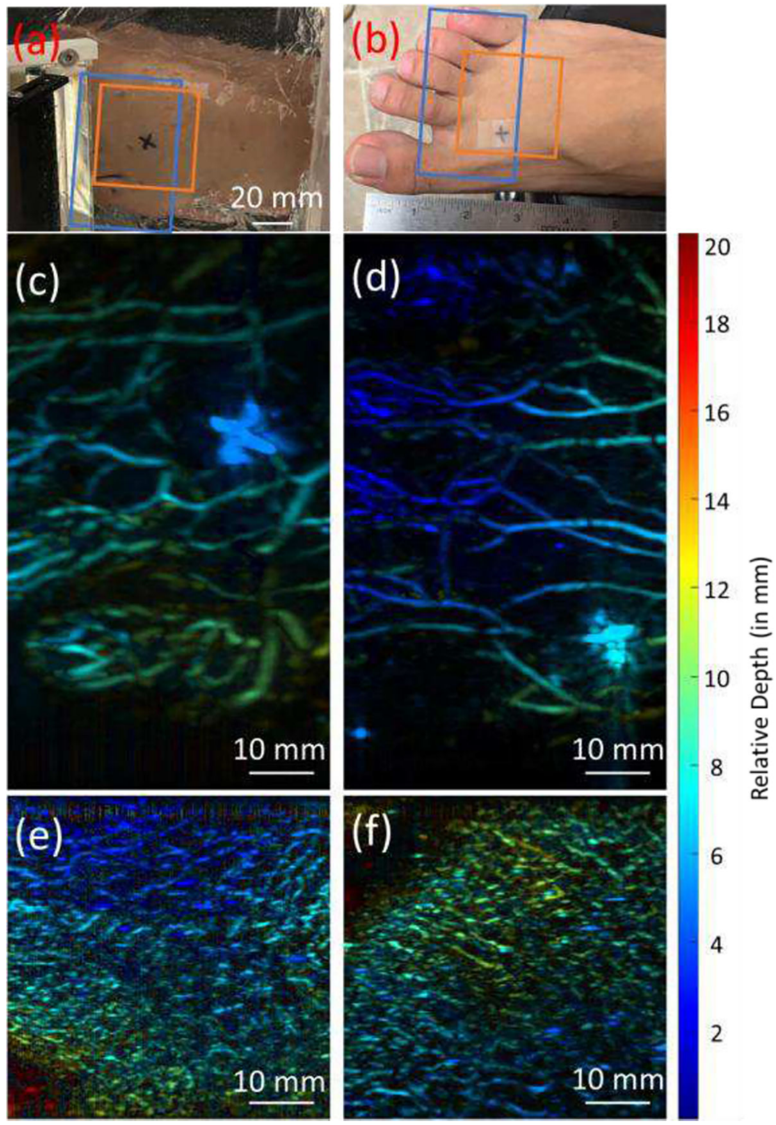

Fig. 6.

In-vivo results from two healthy volunteers. (a) A photograph of the left foot of healthy volunteer 1 (HV01). (b) A photograph of the right foot of healthy volunteer 2 (HV02). (c) The PA depth-encoded MAP image of the dorsal side of the left foot from HV01. (d) The PA depth-encoded MAP image of the dorsal side of the right foot from HV02. (e) The PA depth-encoded MAP image of the plantar side of the left foot from HV01. (f) The PA depth-encoded MAP image of the plantar side of the right foot from HV02. The scanning regions of the top system and bottom system are labeled with blue and orange rectangles, respectively.

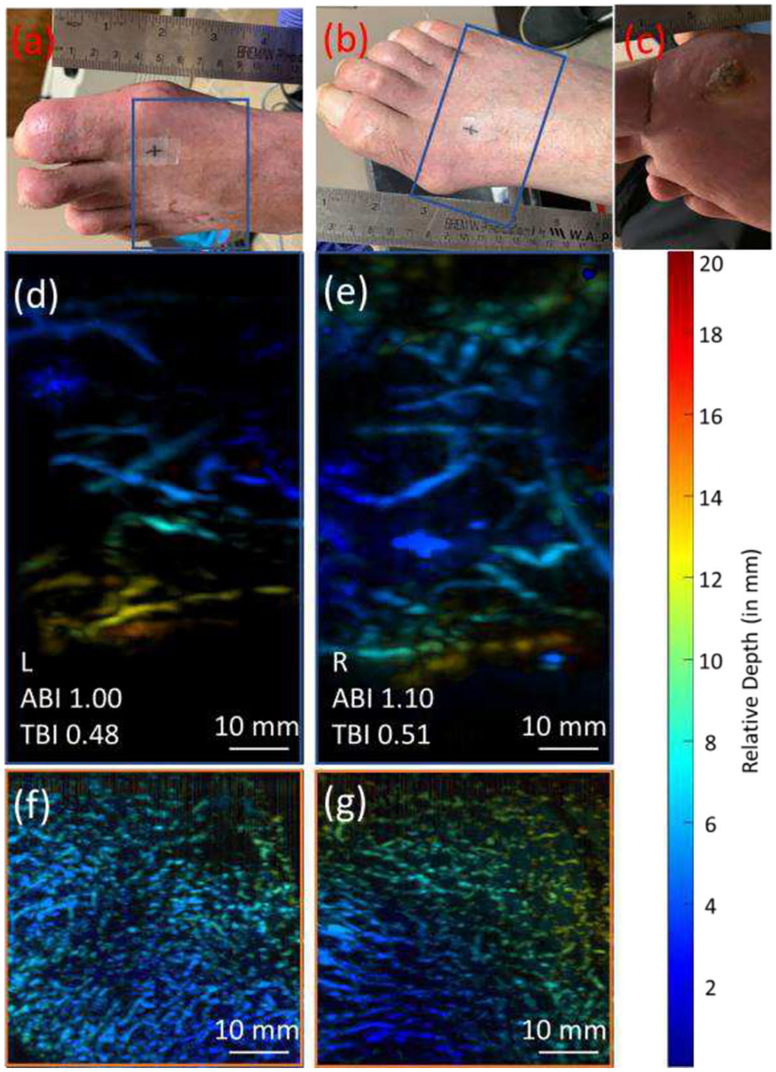

Fig. 7.

In-vivo results from the patient with an ulcer at the plantar side of the left foot. (a) A photograph of the subject's left foot. (b) A photograph of the subject's right foot. (c) A photograph of the ulcer, which is located on the dorsal side of the left foot. (d) The PA depth-encoded MAP image of the dorsal side of the left foot. (e) The PA depth-encoded MAP image of the dorsal side of the right foot. (f) The PA depth-encode MAP image of the plantar side of the left foot. (g) The PA depth-encoded MAP image of the plantar side of the right foot. The imaging region for the top system is labeled with a blue rectangle.

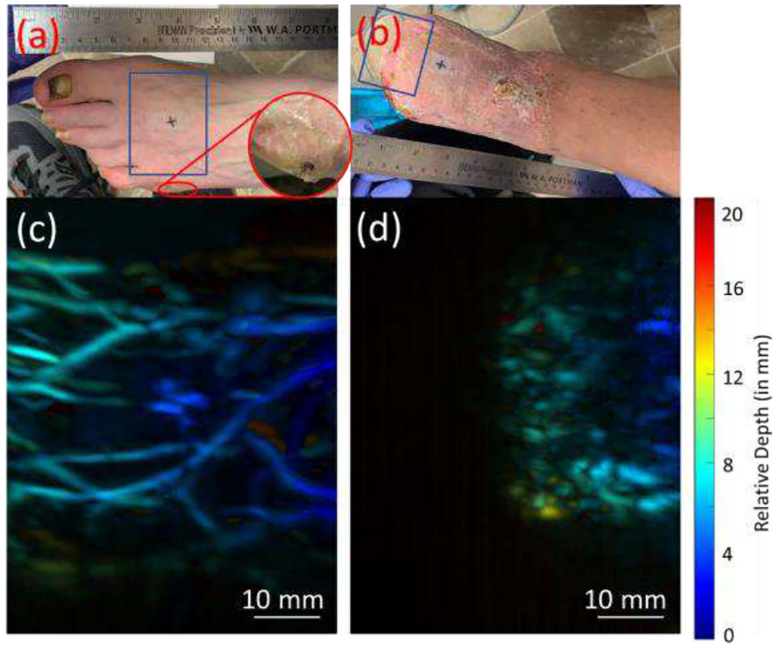

Fig. 8.

In-vivo results of the patient with multiple ulcers on the right foot. The front of the right foot was amputated. (a) A photograph of the patient's left foot. A close look from the side view shows an open wound. (b) A photograph of the patient's right foot, which has been amputated, and multiple ulcers are observed. (c) PA depth-encoded MAP image of the dorsal side of the left foot. (d) PA depth-encoded MAP image of the dorsal side of the right foot.

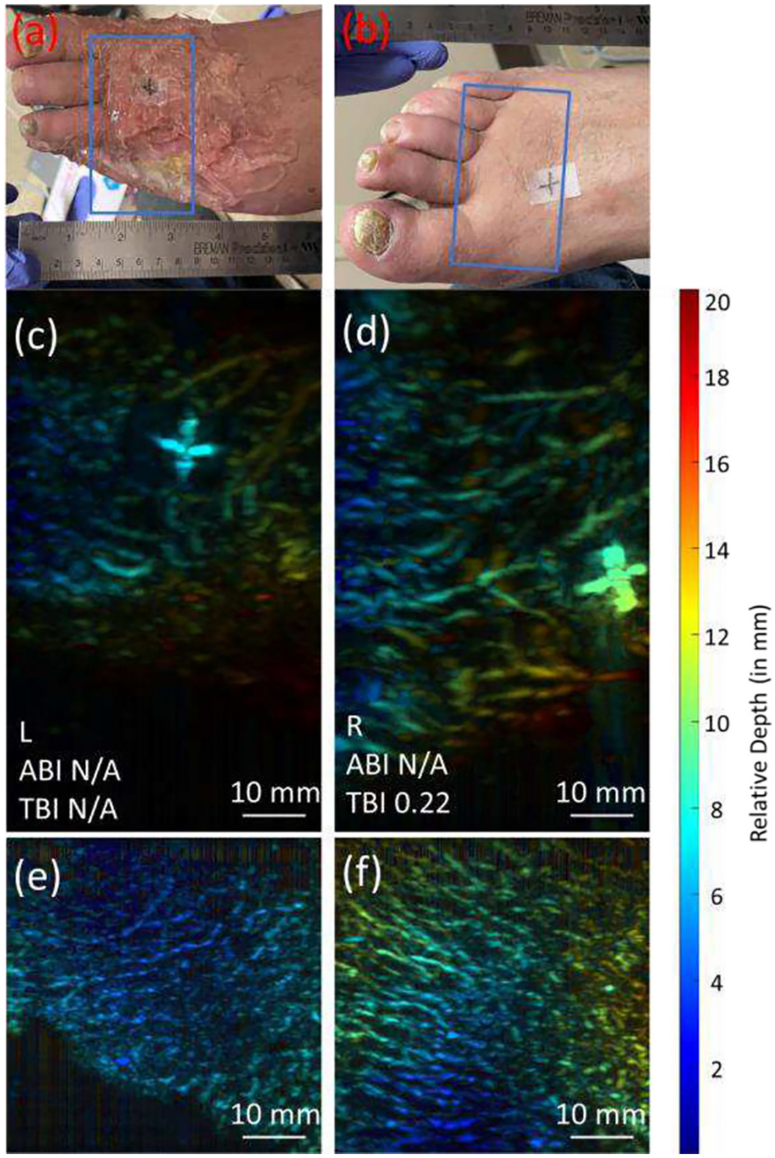

Fig. 9.

In-vivo results of a patient with wounds on the left foot. (a) A photograph of the left foot. Two toes were amputated due to chronic ulcers. (b) A photograph of the right foot (no open wound was observed). (c) PA depth-encoded MAP image of the dorsal side of the left foot. (d) PA depth-encoded MAP image of the dorsal side of the right foot. (e) PA depth-encoded MAP image of the plantar side of the left foot. (f) PA depth-encoded MAP image of the plantar side of the right foot. The scanning regions of the top system are labeled with blue rectangles in photos.

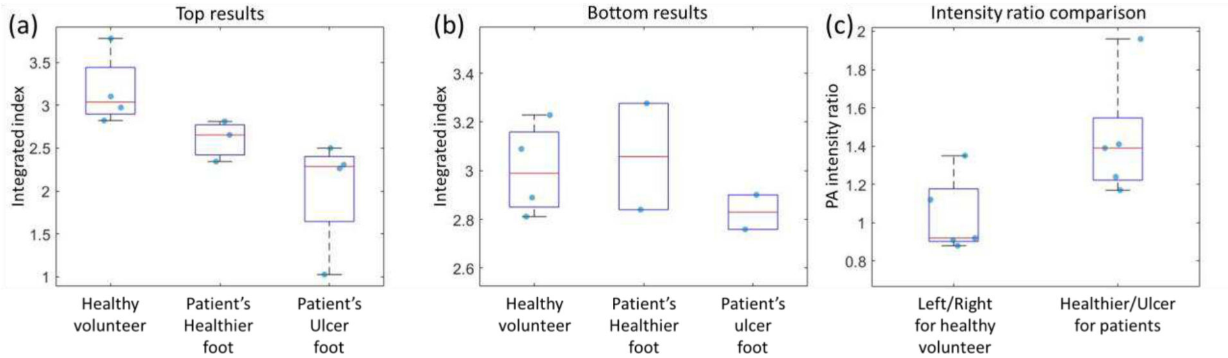

Fig. 10.

Quantitative comparisons between healthy volunteers, healthy feet of the patients, and feet with ulcers of the patients for features acquired by (a) the top system and (b) the bottom system. (c) Comparison of PA intensity ratio between healthy volunteers and patients. The ratio is calculated as Left/Right for healthy volunteers and Healthier foot/Ulcer foot for patients. Data are presented as box plots and data points are marked.

TABLE 1

The vessel features extracted from the healthy volunteers.

Foot	Top		Bottom	
	L (HV01)	**R (HV02)**	**L (HV01)**	**R (HV02)**
Vessel Occupancy	0.39	0.34	0.53	0.47
Sharpness $\times 10^2$	0.49	0.65	0.99	1.07
Vessel Density	2.05	1.82	4.85	3.81
Integrated Index	2.70	2.64	3.23	2.89

TABLE 2

The vessel features extracted from patients 1&2. Patient 1 has wound on the left foot (marked in red). Patient 2 has wound (amputation) on the right foot (marked in red).

Patient Number	Patient 1				Patient 2	
Foot	Top		Bottom		Top	
	L	R	L	R	L	R
PA intensity ratio	1.39		1.24		1.96	
Vessel occupancy	0.33	0.41	0.41	0.31	0.39	0.15
Sharpness $\times 10^2$	0.47	0.46	1.15	1.78	0.30	0.16
Vessel density	1.56	1.92	3.54	2.67	2.10	0.83
Integrated index	2.34	2.73	2.76	2.84	2.50	1.03

TABLE 3

The vessel features extracted from patient 3. The patient has amputation on the left foot (marked in red)

Patient Number	**Patient 3**			
Foot	**Top**		**Bottom**	
	L	**R**	**L**	**R**
PA intensity ratio	1.17		1.41	
Vessel occupancy	0.38	0.38	0.32	0.35
Sharpness $\times 10^2$	0.14	0.15	1.90	2.18
Vessel density	2.15	2.20	2.45	2.75
Integrated index	2.33	2.37	2.90	3.28